Supplementary Information (SI) for Journal of Materials Chemistry C.
This journal is © The Royal Society of Chemistry 2026

Supplementary Information

Deuterium-Enabled Stabilization of Metal/Oxide Interfaces via Suppressed Oxygen Diffusion in BEOL-Compatible InGaZnO Thin-Film Transistors

Woosub Byun[a], Tae-Hyun Kil[b], BongHo Kim[c], Yunseok Kim[d,e], Hwanyeol Park[d,e*], Jun-Young Park[b,f*], Dae-Myeong Geum[a*]

[a] *Department of Electrical and Computer Engineering, Inha University, 100 Inha-ro, Michuhol-gu, Incheon 22212, Republic of Korea*

[b] ParkLab Semiconductor Inc., *1 Chungdae-ro, Seowon-gu, Cheongju-si, Chungcheongbuk-do 28644, Republic of Korea*

[c] *Semiconductor R&D Center, Samsung Electronics, Co. Ltd., Giheung, South Korea*

[d] *Department of Electronic Materials, Devices, and Equipment Engineering, Soonchunhyang University, Asan City, Chungcheongnam-do 31538, Republic of Korea*

[e] *Department of Display Materials Engineering, Soonchunhyang University, Asan City, Chungcheongnam-do 31538, Republic of Korea*

[f] *School of Electronics Engineering, Chungbuk National University, 1 Chungdae-ro, Seowon-gu, Cheongju-si, Chungcheongbuk-do 28644, Republic of Korea*

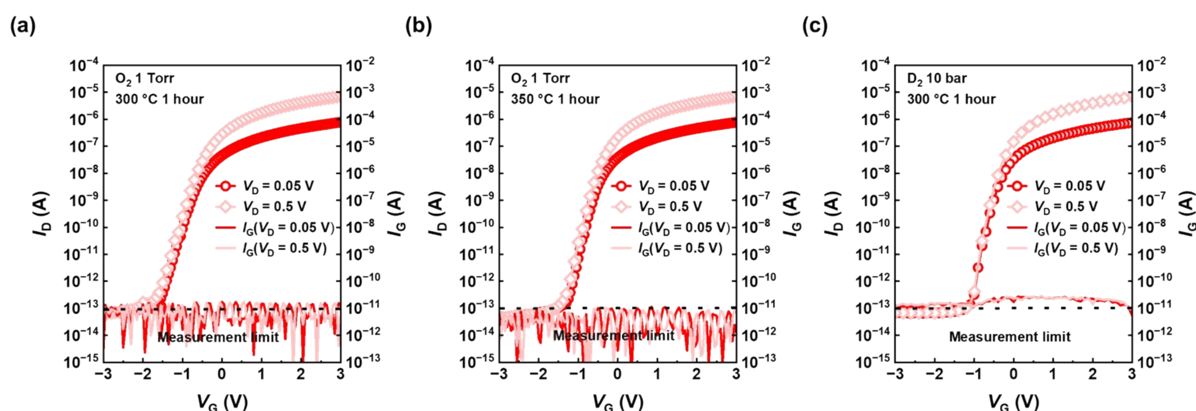

Fig. S1. I_D-V_G curves of a-IGZO TFTs for (a) 300 °C and (b) 350 °C O_2 RTA devices, (c) 300 °C HPDA devices

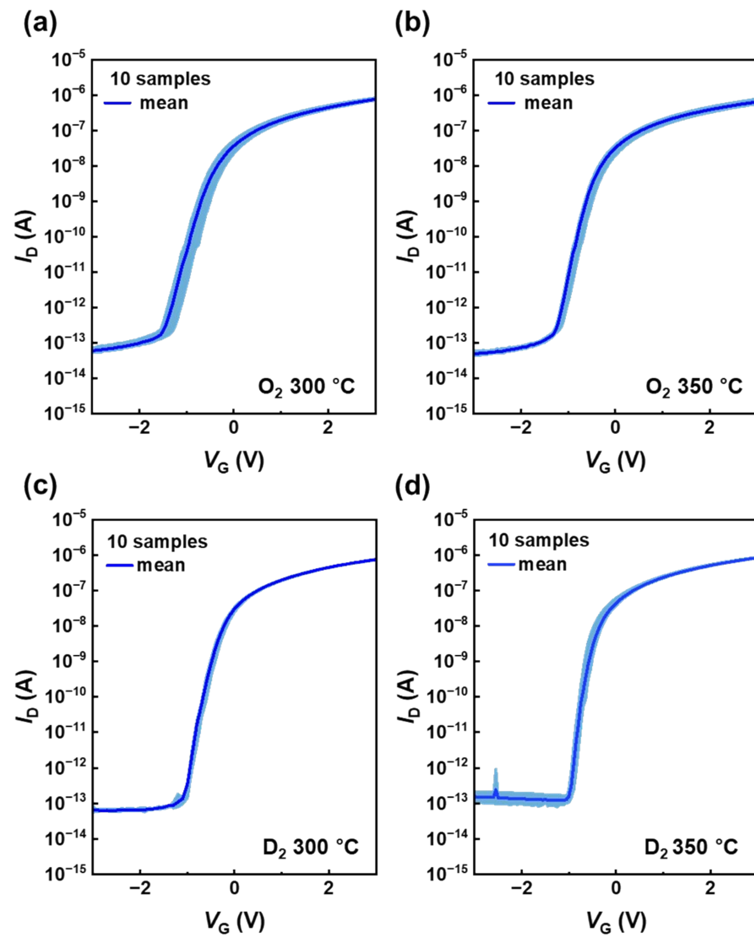

Fig. S2. I_D-V_G curves of a-IGZO TFTs as a function of different annealing ambients by log scale for O_2 (a) 300 °C, (b) 350 °C, D_2 (c) 300 °C and (d) 350 °C: uniformity for sky blue, average for blue lines

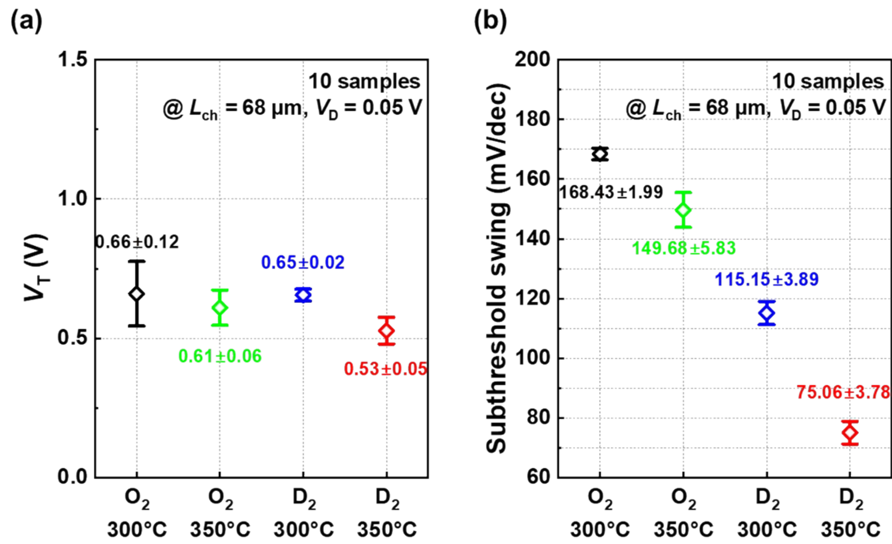

Fig. S3. Box plots of electrical parameters at each temperature (a) V_T and (b) *SS*

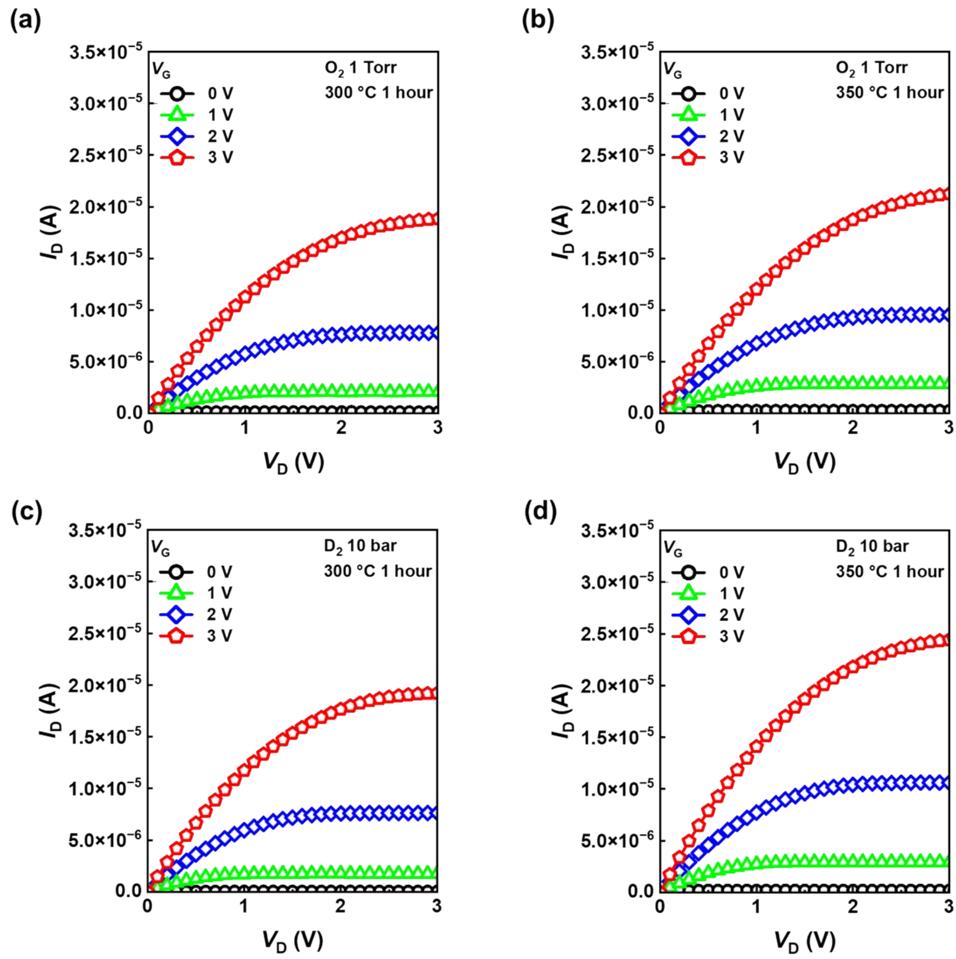

Fig. S4. I_D-V_D curves of a-IGZO TFTs for (a) 300 °C, (b) 350 °C O_2 RTA devices, (c) 300 °C and (d) 350 °C HPDA devices

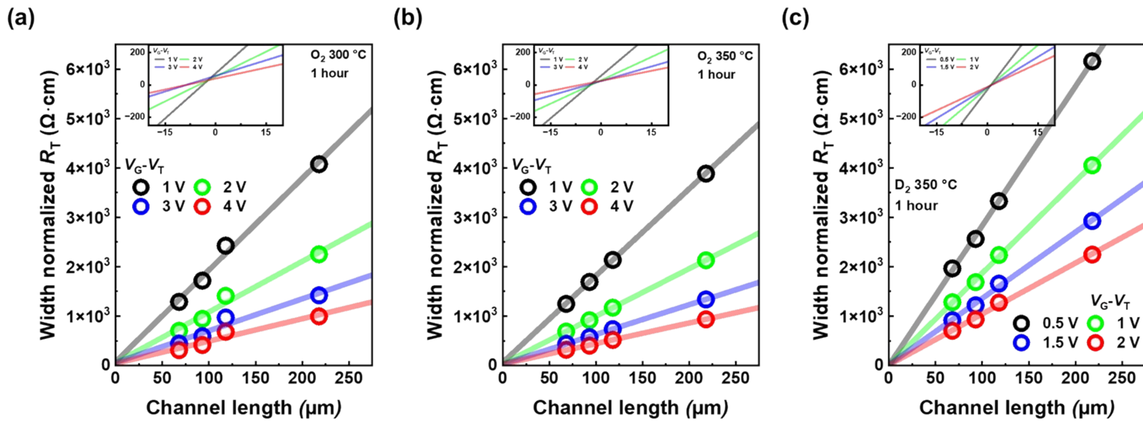

Fig. S5. Graph of width normalized R_T-L obtained by TLM for (a) 300 °C and (b) 350 °C O_2 RTA devices, (c) 300 °C HPDA devices

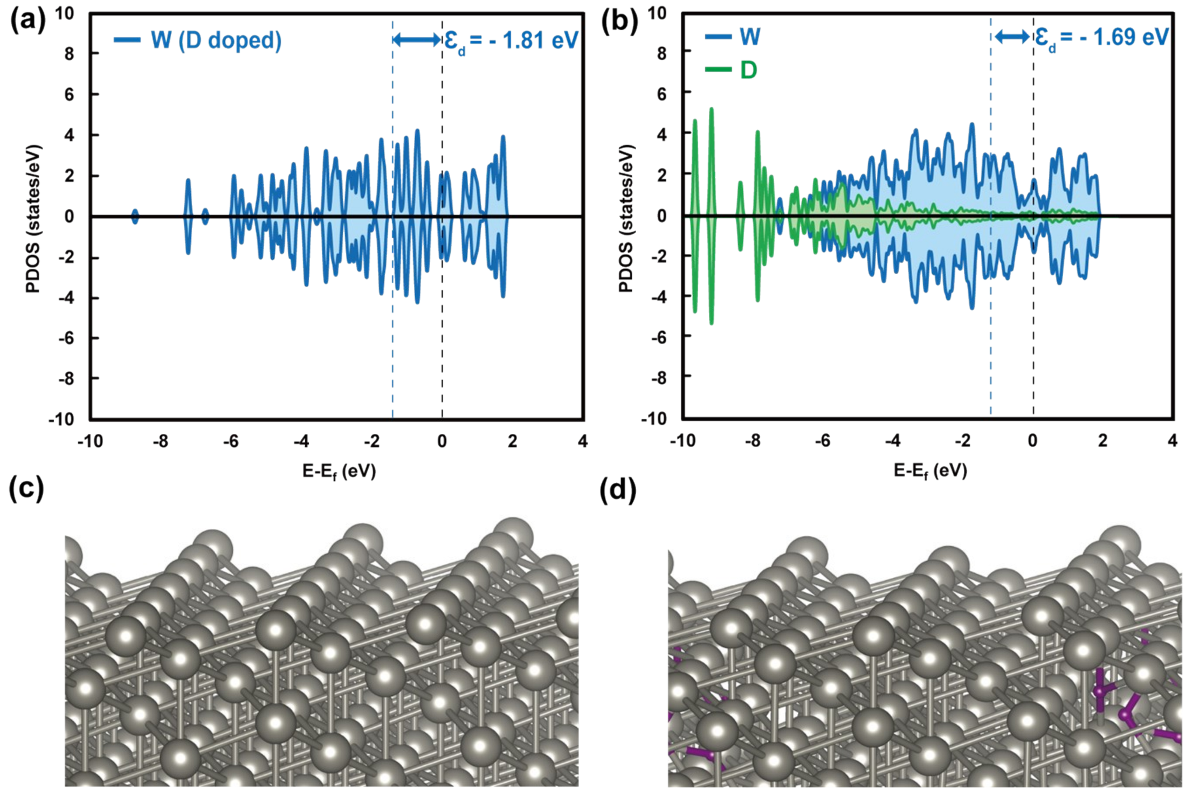

Fig. S6. Partial density of states for the (a) W and (b) W (D doped) structures. (c-d) Side views of the optimized structures.

Amorphous indium gallium zinc oxide (a-IGZO) structures were generated using ab initio molecular dynamics (AIMD) based on a melt–quench procedure,[1] as implemented in the Vienna ab initio Simulation Package (VASP). Starting from a cubic crystalline $InGaZnO_4$ supercell with a lattice size of 13.44 Å, we constructed a 4×4×1 supercell containing 112 atoms. The system was melted at 3000 K for 6 ps to erase crystalline memory and then quenched to 100 K at a cooling rate of 200 K/ps, followed by equilibration at 300 K for 6 ps to obtain an amorphous configuration. This process yields structural characteristics such as coordination environments and radial distribution functions in close agreement with experimental scattering data for sputtered and PLD-grown a-IGZO films.[2] For deuterium-doped amorphous IGZO (a-IGZO:D), ten D atoms were randomly inserted near oxygen-related sites to achieve ~8.2 at% doping, resulting in a total of 122 atoms.

The tungsten electrode was modeled using α-W in a body-centered cubic (BCC) phase with an optimized lattice constant of 3.17 Å, consistent with previous reports. A 3×3×3 supercell was constructed with the (111) surface orientation exposed, resulting in a slab containing 72 atoms. For interface models, the W slab was placed in contact with the amorphous IGZO slab (with or without D), producing heterostructures composed of 184 atoms (W/a-IGZO) and 194 atoms (W/a-IGZO:D). A vacuum region of 15 Å was introduced along the surface normal to avoid spurious periodic interactions.

All AIMD and DFT calculations were carried out using the projector-augmented wave (PAW) method [3] within the generalized gradient approximation (GGA) [4] using the Perdew–Burke–Ernzerhof (PBE) exchange-correlation functional. A plane-wave cutoff energy of 400 eV was applied, and the Brillouin zone was sampled at the Γ-point during AIMD simulations, while a 3×3×3 Monkhorst–Pack mesh was employed for static relaxations and density of states calculations. Structural relaxations were converged until the forces on each atom were less than 0.02 eV/Å. AIMD simulations were performed in the NVT ensemble using a Nosé–Hoover thermostat with a 1 fs time step, consistent with previous melt–quench simulations of amorphous oxides.

The interfacial adhesion strength was evaluated by calculating the interfacial energy, defined as:

$$E_{\mathrm{int}} = [\mathrm{E}_{\mathrm{W/a\text{-}IGZO}} - (E_{\mathrm{W}} + E_{\mathrm{a\text{-}IGZO}})]/S$$

where $E_{\mathrm{W/a\text{-}IGZO}}$ is the total energy of the heterostructure, E_{W} and $E_{\mathrm{a\text{-}IGZO}}$ are the energies of the isolated slabs with identical thicknesses, and S is the interfacial area. Negative values of E_{int} indicate stronger adhesion and improved interfacial stability.

To investigate ion migration, the climbing-image nudged elastic band (CI-NEB) method [5] was employed to compute minimum energy pathways for oxygen and deuterium diffusion across the W/a-IGZO interface. Diffusion barriers were obtained from the energy difference between the initial and transition states along the identified pathways. Charge transfer analyses were carried out by calculating charge density difference (CDD) maps and Bader charge partitioning, allowing for a quantitative evaluation of electron redistribution across the interface. Additionally, the partial density of states (PDOS) was computed to identify orbital hybridization between W and IGZO atoms, while the d-band center of W was extracted to assess changes in bonding activity upon deuterium incorporation.

This integrated computational framework—combining AIMD for amorphous structure generation, DFT for energetics and electronic structure, and NEB for diffusion kinetics—provides a consistent atomistic picture of how deuterium incorporation enhances interfacial adhesion, suppresses oxygen diffusion, and modifies the electronic structure of W/a-IGZO heterostructures.

S/D electrode	Year [Ref]	interlayer	Structure	Gate insulator	Annealing temperature	Channel deposition	SS (mV/dec)	μ_{FE} ($cm^2/V{\cdot}s$)	R_CW ($\Omega{\cdot}cm$)	ΔL (μm)
W	**Our work**	**-**	**Back gate**	**Al_2O_3 / 15 nm**	**D_2 350 °C 1 hr**	**Sputtering**	**74**	**10.78**	**5.74**	**1.51**
	2022 [6]	-	Back gate	SiO_2 / 30 nm	air 400 °C 1 hr / air 150 °C 30 min	Sputtering	130	24.52	4	-
	2024 [7]	TiN	Back gate	Al_2O_3 / 15 nm	O_2 350 °C 1 hr	PVD	76	4.65	14.9	-
ITO	2024 [8]	IGTO/TiN	Back gate	SiO_2 / 100 nm	air 500 °C 1 hr	ALD	100	45	0.7	-
	2022 [9]	-	Top gate	Al_2O_3 / 80 nm	X	ALD	200	36.9	1.8	0.4
	2019 [10]	W	Back gate	SiO_2 / 40 nm	N_2 360 °C 30 min	Sputtering	-	8.5	2.7	0.04
	2024 [11]	AZO	Back gate	SiO_2 / 100 nm	air 500 °C 1 hr	ALD	100	45.3	0.13	-
n^+ IGZO	2023 [12]	-	Top gate	Al_2O_3 / 40 nm	UV irradiation	ALD	181	23.43	8.5	1.17
Pd	2024 [13]		Back gate	SiO_2 / 150 nm	300 °C 1 hr / H_2 200 °C 10 min	Sputtering	-	20	5.9	0.82
	2018 [14]	Ti	Back gate	Ta_2O_5 / 120 nm	air 200 °C 30 min	Sputtering	-	18.2	9.53	-
Ti	2021 [15]	-	Back gate	SiO_2	air 200 °C 30 min	Sputtering	1200	4.25	430	-
Mo	2015 [16]	-	Back gate	SiN_x / SiO_2 100 / 40 nm	N_2 300 °C 1 hr / UV irradiation	Sputtering	210	6.7	27	0.4
	2025 [17]	-	Top gate	Al_2O_3 / 25 nm	180 °C 2 hr	Sputtering	105	10.1	1.53	0.16
	2021 [18]	-	Top gate	SiO_2 / 100 nm	vacuum 350 °C 2 hr / UV irradiation	ALD	360	20.1	9.4	0.1
Au	2025 [19]	ZnO/TiN	Back gate	SiO_2 / 90 nm	air 380 °C 30 min	Sputtering	555	-	1.12	-
	2024 [20]	ITO	Back gate	Al_2O_3	Rapid photonic annealing	Solution	80	3.56	180	-
	2022 [21]	Ti	Top gate	Al_2O_3 / 30 nm	air 180 °C 2 hr	Sputtering	94.16	23.06	10.5	0.88
Cu	2018 [22]	ITO	Back gate	Al_2O_3 / 200 nm	air 450 °C 1 hr / Ar 300 °C 1hr	Sputtering	200	11.5	18	-
	2021 [23]	MoTi	Back gate	SiO_2 / 100 nm	air 400 °C 15 min	Sputtering	410	14.8	105	-
Al	2025 [24]	-	Back gate	SiO_2 / 100 nm	150 °C 1 hr	sputtering	270	12.19	0.4	-
Ni	2019 [25]	-	Back gate	SiO_2 / 100 nm	N_2 400 °C 30 min	Sputtering	220	11.76	1513	4.29
Pt	2007 [26]	-	Back gate	SiN_x / 200 nm	Ar plasma treatment	Sputtering	190	9.1	330	-

Table S1. Comparison of reported IGZO TFT performances

References

1. G. Kresse and J. Hafner, *Phys. Rev. B*, 1993, 47, 558–561.
2. B. Cui, L. Zeng, D. Keane, M. J. Bedzyk, D. B. Buchholz, R. P. H. Chang, X. Yu, J. Smith, T. J. Marks, Y. Xia, A.F. Facchetti, J.E. Medvedeva and M. Grayson, *J. Phys. Chem. C*, 2016, 120, 7467–7475.
3. G. Kresse and J. Furthmüller, *Phys. Rev. B*, 1996, 54, 11169–11186.
4. J. P. Perdew, K. Burke and M. Ernzerhof, *Phys. Rev. Lett.*, 1996, 77, 3865–3868.
5. G. Henkelman and H. Jónsson, *J. Chem. Phys.*, 2000, 113, 9978–9985.
6. M. J. Kim, H. J. Park, S. Yoo, M. H. Cho and J. K. Jeong, *IEEE Trans. Electron Devices*, 2022, 69, 2409–2416
7. H. Tang, H. Dekkers, N. Rassoul, S. Sutar, S. Subhechha, V. Afanas'ev, J. Van Houdt, R. Delhougne, G. S. Kar and A. Belmonte, *IEEE Trans. Electron Devices*, 2024, 71, 567–573.
8. J. H. Jeong, S. W. Seo, D. Kim, S. H. Yoon, S. H. Lee, B. J. Kuh, T. Kim and J. K. Jeong, *Sci. Rep.*, 2024, 14, 10953.
9. D. H. Lee, Y. H. Kwon, N. J. Seong, K. J. Choi, G. Kim and S. M. Yoon, *ACS Appl. Electron. Mater.*, 2022, 4, 6215–6228.
10. J. Kataoka, N. Saito, T. Ueda, T. Tezuka, T. Sawabe and K. Ikeda, *Jpn. J. Appl. Phys.*, 2019, 58, SBBJ03.
11. J. H. Jeong, S. H. Yoon, S. H. Lee, B. J. Kuh, T. Kim and J. K. Jeong, *IEEE Electron Device Lett.*, 2024, 45, 849–852.
12. S. H. Moon, Y. H. Kwon, N. J. Seong, K. J. Choi and S. M. Yoon, *IEEE Electron Device Lett.*, 2023, 44, 1128–1131
13. Y. Shi, M. Tsuji, H. Cho, S. Ueda, J. Kim and H. Hosono, *ACS Nano*, 2024, 18, 9736–9745.
14. Y. Wang, J. Yang, H. Wang, J. Zhang, H. Li, G. Zhu, Y. Shi, Y. Li, Q. Wang, Q. Xin, Z. Fan, F. Yang and A. Song, *IEEE Trans. Electron Devices*, 2018, 65, 1377–1382.
15. J. Seo and H. Yoo, *Micromachines*, 2021, 12, 481.
16. M. M. Kim, M. H. Kim, S. M. Ryu, J. H. Lim and D. K. Choi, *RSC Adv.*, 2015, 5, 82947–82951.
17. C. Chen, X. Duan, C. Lu, X. Chuai, W. Wu, C. Zhang, C. Gu, G. Yang, N. Lu, D. Geng and L. Li, *IEEE J. Electron Devices Soc.*, 2025, 13, 135–138.

18. D. G. Kim, S. H. Ryu, H. J. Jeong and J. Park, *ACS Appl. Electron. Mater.*, 2021, 3, 3530–3537.

19. S. Song, J. H. Kim, J. Park, S. H. Kim, D. Ko, H. Choi, S. Kim and H. Yu, *Appl. Surf. Sci. Adv.*, 2025, 25, 100676.

20. L. Luo, H. Faber, C. Liu, S. Doukas, E. Yarali, B. Adilbekova, D. R. Naphade, N. Xiao, Y. Ma, H. F. Mazo Mantilla, L. Panagiotidis, W. S. Alghamdi, C. F. Florica, M. I. Nugraha, X. Li, X. Zhang, M. Heeney, E. Lidorrikis and T. D. Anthopoulos, *Adv. Funct. Mater.*, 2024, 34, 2406044.

21. X. Duan, C. Lu, X. Chuai, Q. Chen, G. Yang and D. Geng, *Micromachines*, 2022, 13, 652.

22. S. Hu, K. Lu, H. Ning, Z. Fang, X. Liu, W. Xie, R. Yao, J. Zou and M. Xu, *IEEE Electron Device Lett.*, 2018, 39, 504–507.

23. J. L. Kim, C. K. Lee, M. J. Kim, S. H. Lee and J. K. Jeong, *Thin Solid Films*, 2021, 731, 138759.

24. J. Sun, T. Jin, M. Lei, Z. Fu, Z. Chen, J. Ren, H. Chen, L. Liang and H. Cao, *ACS Appl. Electron. Mater.*, 2025, 7, 2894–2900.

25. J. W. Choi, S. H. Park, C. G. Yu, W. J. Cho and J. T. Park, *Microelectron. Reliab.*, 2019, 100–101, 113416.

26. J. S. Park, J. K. Jeong, Y. G. Mo, H. D. Kim and S. I. Kim, *Appl. Phys. Lett.*, 2007, 90, 262106.